UNIVERSITY OF TWENTE.

Faculty of Engineering Technology

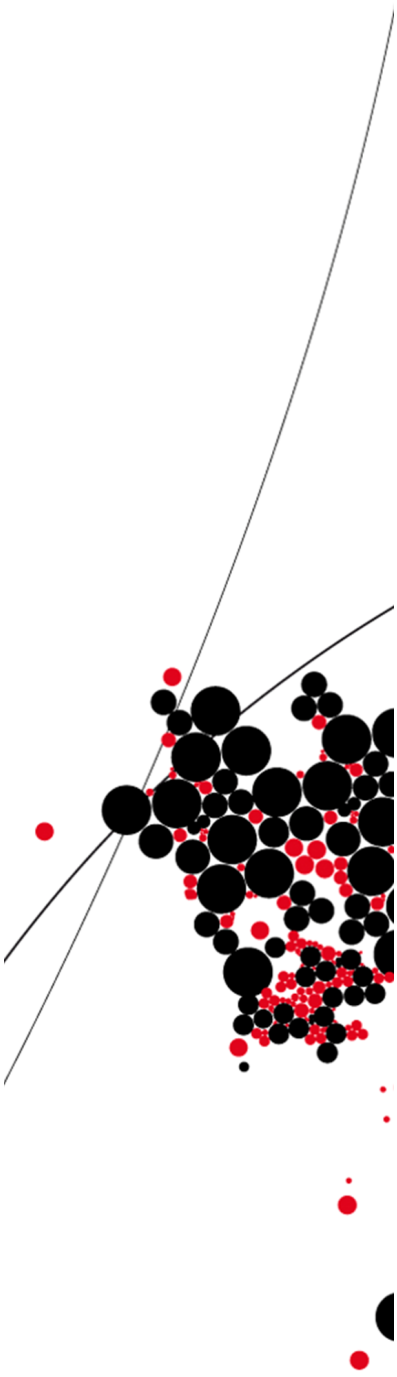

Entropy-patch choked-nozzle interaction: matching-condition and inertial-effects regimes mapped & preliminary investigations of amplitude effects

K. Kowalski

MSc Thesis Assignment
Mechanical Engineering: Energy & Flow
July 2024

Document number:
EFD-447

Exam Committee:
prof. dr. ir. C.H. Venner (chair)
prof. dr. ir. H. Askes (external member)
dr. ir. J.A.M. Withag (internal member)
dr. ir. L. Hirschberg (supervisor)

Faculty of Engineering Technology
Chair of Engineering Fluid Dynamics
University of Twente
P.O. Box 217
7500 AE Enschede
The Netherlands

Contents

I. Introduction

A. Thermo-acoustic instability

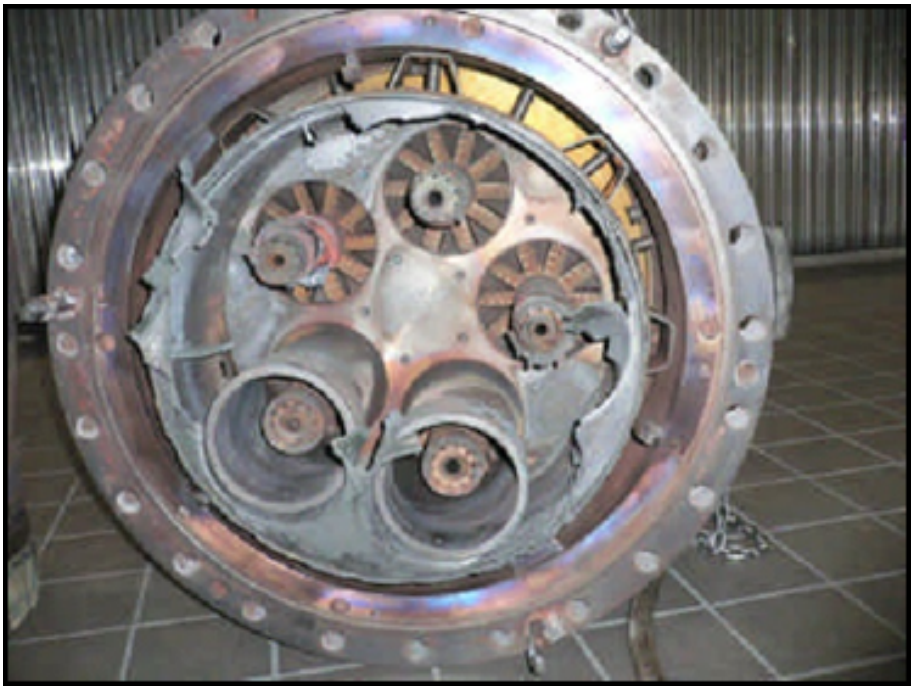

Fig. 1 Land based gas turbine GE frame 9 combustor can with 5 burners severely damaged due to thermoacoustics (courtesy of J.B.W. Kok)

Fig. 1 is an image of a land based gas turbine which has suffered catastrophic failure; the reason for said failure is attributed to thermo-acoustic instability. In its essence, thermo-acoustic instability reduces to a feedback loop of sound sources coupling with the combustion-chamber acoustics of the system. Under unfavourable circumstances, this leads to self-sustained pressure pulsations. The sound sources which lead to thermo-acoustic instability are commonly referred to as combustion noise. Combustion noise may be categorized in:

1) Direct combustion noise
2) Indirect combustion noise

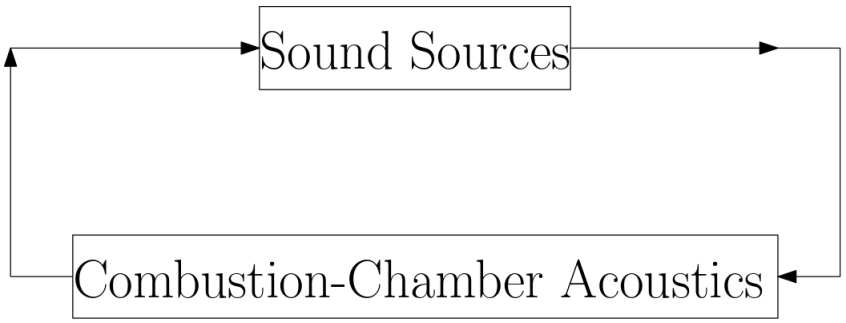

Fig. 2 Feedback loop in self-sustained pressure pulsations

Direct combustion noise arises from unsteady volumetric gas expansion/contraction in flames [1]. This leads to the generation of acoustic waves, which is termed "direct combustion noise".

Indirect combustion noise refers to flow inhomogeneities interacting with a combustion chamber exit. Indirect combustion noise is further categorized in:

- vorticity noise
- entropy noise

Vorticity noise refers to the interaction of vortices with the combustion chamber exit. Entropy noise, which is the *focus of this research assignment*, refers to the interaction of entropy patches with the combustion chamber exit. An entropy patch is a region in the flow where the thermodynamic state is locally appreciably different from the surrounding flow. Entropy patches are thought to be a consequence of an unsteady rate of heat release, which would e.g. cause temperature/density inhomogeneities in the main flow. Said patches are carried downstream atop the main flow, as these exit, sound waves are generated [1].

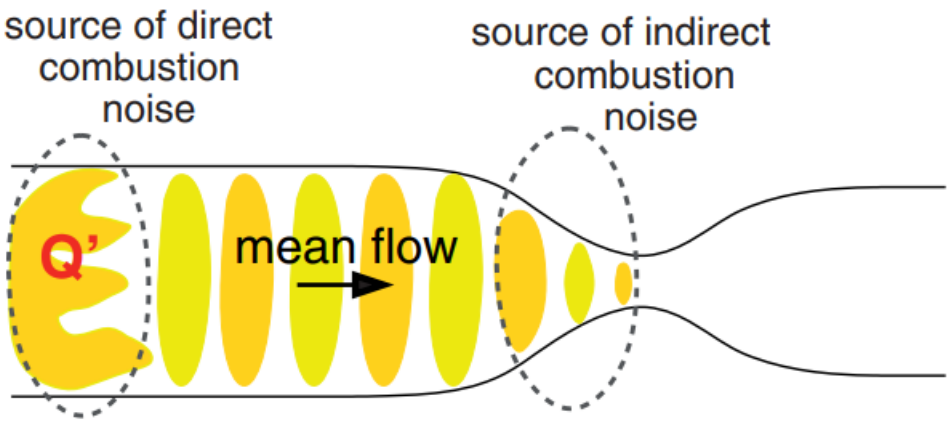

Fig. 3 Sources of combustion noise for combustion chamber with a nozzle exit (figure taken from [1])

A part of these sound waves propagates downstream, whereas others are reflected back upstream. Upstream travelling waves may induce further entropy patches upstream which, upon exiting the chamber: generate further sound waves propagating back upstream.

Entropy noise is asserted to be an issue in aero-engines & gas-turbines [1]. Whereas vorticity noise is an established problem in solid rocket motors (SRMs) [2–7].

Dowling and Mahmoudi [8] assert that combustion noise has been of increasing importance in recent years in comparison to other noise sources, especially in aero-engines & land based gas turbines. This is in part attributed to recent efforts to reduce aircraft noise, particularly jet noise reduction [9]. Nevertheless, combustion noise has also seen an increasing interest as newer generation combustor systems burn more unsteadily, thus increasing the effects of combustion noise [8]. Additionally, growing environmental concerns associated with aero-engines further emphasizes

the growing research in combustion noise. This is best seen by some of the ACARE Flightpath 2050 goals; amongst these is the goal to reduce NO_x emissions by 90% [10]. In order to achieve this, systems employing a lean premixed combustion is often preferred. The disadvantage to using a lean premixed combustion is that it is more susceptible to combustion noise as it burns in a more unsteady manner [8, 9] thus reinforcing the growing need to appropriately address combustion noise.

B. Modeling approaches for entropy noise found in the literature

1. Matching-condition/Marble-Candel-like modeling

Marble & Candel [11] provide useful insights as to the acoustic disturbances generated by entropy patches through a nozzle. Through their 1D modelling approach, they investigated the effects of entropy patches convected through compact & extended nozzles. Compact nozzles refer to the case where the impinging disturbances are of wavelengths much longer than the length of the nozzle. Conversely, extended nozzles, have a nozzle length longer than the wavelengths of said disturbances. In both instances, it has been demonstrated that entropy patches play a key role in sound production.

Most interesting is their observation on the application of quasi-steady modelling. It has been shown that for compact nozzles, that is to say, a nozzle whom's length is small compared to the scale of the disturbance impinging upon it, the acoustic disturbance may be modelled under quasi-steady assumptions. More specifically, Marble & Candel have stated "When the scale of the disturbance impinging upon the nozzle is large in comparison with the nozzle length (that is, the reduced frequency of the system is low), the response of the nozzle is well approximated by a quasi-steady analysis. Though limited in the range of frequency over which it is applicable, the results which follow from this approximation are simple and extremely useful. The idea is simply that, to disturbances of very long wavelength, the nozzle appears as a discontinuity in the state of the medium supporting the propagation. The nozzle then provides matching conditions, between uniform upstream and downstream states, which may be derived from conservation laws and the geometric description of the nozzle." [11].

From a modeling perspective, the nozzle is reduced to a single point on an axis where the thermodynamic state upstream & downstream of this point are different, the nozzle provides matching conditions between these states.

2. Inertial-effect/Ffowcs-Williams-Howe-like modeling

The work of Ffowcs Williams & Howe involves sound generation due to density inhomogeneities in low Mach nozzle flows [12]. A 3D analytical model is developed to determine sound generation due to: the passage of an *entropy slug* (a relatively large entropy patch) & a smaller spherical *pellet*. In their model, the acceleration of these inhomogeneities are explicitly modeled, moreover, said models predict that "the radiated pressure levels are negligible unless the source, which is attached to a fluid particle, is itself accelerating, e.g. through a region of non-uniform mean flow, in which case the dominant radiation may be termed *acoustic bremsstrahlung*" [12]. Moreover, the argument

made seems to be that "to elicit in detail the physical mechanisms responsible for the generation of sound" the inclusion of acceleration/unsteadiness is fundamental.

3. Comment re state-of-the-art

In I.B.1 & I.B.2, two of the most seminal articles related to entropy noise have been summarized. In one case, Marble & Candels' quasi-steady analysis (where the nozzle provides matching-conditions) is applied to model entropy-patch choked-nozzle interactions (ECNI), conversely, the work of Ffowcs Williams & Howe models acceleration and seems to argue that acceleration of flow inhomogeneities is a fundamental mechanism for sound production. Moreover, majority of the research conducted following these seminal articles involves nuanced versions of Marbel & Candels' quasi-steady analysis where, despite the use of a quasi-steady analysis, it is argued that the acceleration of *entropy waves* is the source of entropy noise in combusting flows.

Clearly, there are inconsistencies in the field regarding the mechanism responsible for sound production in entropy noise. The general argument that acceleration of entropy waves generates entropy noise implies, from a modeling perspective, that modeling the acceleration term is paramount to capturing the physics of the problem. However, what is observed in the literature, is the use of quasi-steady (matching-condition modeling), where acceleration is not explicitly modeled. Moreover, one may note that the definition of an entropy wave is rather vague, and may argue that, for applications in a combustion chamber, it is more intuitive to refer to these inhomogeneities as entropy patches which have a specified shape and streamwise lengthscale.

C. Focus of the Study

Based on the inconsistencies discussed in I.B.3, but with a focus on choked-nozzle flow, the influence of an entropy patch's shape and more importantly its size on: the upstream-travelling acoustic response due to the passage of an entropy patch is discussed in the presently reported work *. Moreover, the limits of the matching-condition & inertial modeling (where inertial effects, i.e. acceleration, play a dominant role on the upstream acoustic response) regime are established.

II. Theory

In this section, two models are developed for the prediction of the upstream acoustic response due to an entropy patch interacting with a choked nozzle. The first model is a matching-conditions model inspired by Marbel & Candel where acceleration is not modelled. The second model presented in this section is an inertial-effects model, where the steady convective acceleration of entropy patches is explicitly modeled.

*The presently reported work is an extended version of the paper published by AIAA, available at [13]

A. Quasi-1-D Matching-conditions model

In the following, a model (inspired by the quasi-steady analysis of Marble & Candel [11]) is derived for the upstream observed acoustic pressure response p'_{u}, due to the interaction of an entropy patch of relative excess density $\rho_e/\bar{\rho} \equiv (\rho - \bar{\rho})/\bar{\rho}$ with a choked nozzle. Here ρ and $\bar{\rho}$ are the density with and without the presence of an entropy patch, respectively. The (unperturbed) base flow carrying the entropy patch is taken to be steady. One assumes that $\rho_e/\bar{\rho}$ is small enough, such that the entropy patch is carried by the base flow without affecting it. Upstream from the nozzle, the flow is taken to be one-dimensional (1D); namely, the local flow variables vary only in the axial direction and are taken to be locally uniform over a cross section at any particular axial position x. Furthermore, it is assumed that the interaction-time scale of the entropy patch with the nozzle is significantly larger than the travel time of a material element through the nozzle.

The local base flow Mach number M is defined as:

$$M \equiv \frac{u}{c} \tag{1}$$

where u and c are the local flow velocity and speed of sound, respectively. For a choked nozzle, M upstream is contant, and in this case, the upstream Mach number is set to 0.2. Hence, for the perturbations of the base flow velocity u' and speed of sound c', upstream one has:

$$M = \frac{u}{c} = 0.2 \tag{2}$$

Taking the natural logarithm and differentiating:

$$\ln(M) = \ln(0.2) \tag{3}$$

$$\mathrm{d}\ln(u) - \mathrm{d}\ln(c) = \mathrm{d}\ln(0.2) \tag{4}$$

$$\frac{c'}{c} = \frac{u'}{u} \tag{5}$$

Assuming the fluid is a calorically perfect gas, one has

$$c^2 = \gamma \frac{p}{\rho} \tag{6}$$

Taking the natural logarithm and differentiating:

$$\ln(c^2) = \ln\left(\gamma \frac{p}{\rho}\right) \tag{7}$$

$$2\ln(c) = \ln(\gamma) + \ln(p) - \ln(\rho) \tag{8}$$

Assuming the formation of an entropy patch of relative excess density $\rho_e/\bar{\rho}$ at constant pressure (isobaric process), one finds

$$\mathrm{d}2\ln(c) = \cancel{\mathrm{d}\ln(\gamma)} + \cancel{\mathrm{d}\ln(p)} - \mathrm{d}\ln(\rho) \tag{9}$$

$$\frac{\rho_e}{\bar{\rho}} = -2\frac{c'}{c} \tag{10}$$

Substituting Eqs. (5) & (1):

$$\frac{\rho_e}{\bar{\rho}} = \frac{-2u'}{Mc} \tag{11}$$

$$\frac{c\rho_e}{2\bar{\rho}} = \frac{-u'}{M} \tag{12}$$

Rearranging for u'

$$u' = \frac{1}{2}\left(\frac{\rho_e}{\bar{\rho}}\right)Mc \tag{13}$$

Taking the positive flow direction to be from upstream to downstream, and assuming a semi-infinitely long uniform duct upstream from the nozzle with an upstream non-reflecting boundary condition, the acoustic pressure perturbation p'_u observed upstream is

$$p'_u = p^-_u + \cancel{p^+_u} = -\bar{\rho}cu' = \frac{1}{2}\left(\frac{\rho_e}{\bar{\rho}}\right)Mc^2\rho \tag{14}$$

$$\boxed{p'_u = \frac{1}{2}\left(\frac{\rho_e}{\bar{\rho}}\right)\gamma pM} \tag{15}$$

where $p = \rho c^2/\gamma$ is the static pressure of the flow at the nozzle inlet. This result will be referred to as the matching-conditions model, in the remainder of the text. The relation $p'_u = -\rho cu$ will now be explained in more detail. The relation is centred on d'Alembert's solution to the one-dimensional wave equation. According to this solution, a pressure perturbation may be written as:

$$p' = \cancel{p^+(x - ct)} + p^-(x + ct) \tag{16}$$

and similarly, a velocity perturbation:

$$u' = \cancel{u^+(x - ct)} + u^-(x + ct) \tag{17}$$

Looking at the linearized one-dimensional momentum conservation equation:

$$\bar{\rho}\frac{\partial u'}{\partial t} = -\frac{\partial p'}{\partial x} \tag{18}$$

Applying the pressure & velocity perturbations to the linearized one-dimensional momentum equation yields

$$p^{\pm} = \pm\bar{\rho}cu^{\pm} \tag{19}$$

which is what has been applied to derive the matching-condtions model.

B. Quasi-1-D point-mass model

Consider a sound source in the form of a fluctuating pressure discontinuity Δp at position $x = x_s$ in a duct of uniform cross-section with a uniform 1D flow with Mach number M. In the case of an isentropic flow the amplitudes of plane acoustic pressure $p^{\pm}$ and density waves $\rho^{\pm}$, are related as follows:

$$p^{\pm} = c^2\rho^{\pm} \tag{20}$$

where the superscripts + or − indicate a plane wave traveling in the positive or negative direction with respect to the uniform 1D base flow. Taking $p = p(\rho, s)$, the total differential is:

$$\mathrm{d}p = \left(\frac{\partial p}{\partial \rho}\right)_s \mathrm{d}\rho + \left(\frac{\partial p}{\partial s}\right)_\rho \mathrm{d}s \tag{21}$$

For an isentropic flow:

$$\mathrm{d}p = \left(\frac{\partial p}{\partial \rho}\right)_s \mathrm{d}\rho + \cancel{\left(\frac{\partial p}{\partial s}\right)_\rho \mathrm{d}s} = \mathrm{d}p = c^2\mathrm{d}\rho \tag{22}$$

Moreover, recalling Eq. (19), for the acoustic velocity waves $u^{\pm}$, one has

$$u^{\pm} = \pm\frac{p^{\pm}}{\bar{\rho}c}. \tag{23}$$

As sketched in Fig. 4, two plane waves are generated on either side of the pressure discontinuity: p_u^+ and p_d^-, where the subscripts u and d stand for up- and downstream, respectively. Assuming anechoic duct terminations, one can express Δp in terms of the acoustic pressure waves emanating from it:

$$\Delta p = p_d^+ - p_u^-. \tag{24}$$

Across the pressure discontinuity, the mass flux ρu is conserved:

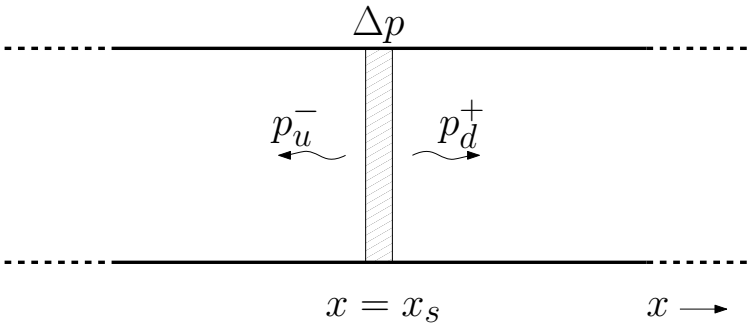

Fig. 4 Fluctuating pressure discontinuity Δp at $x = x_s$, in a uniform 1D ducted flow. Plane acoustic pressure waves: p_u^- and p_d^+ emanate from Δp in the up- and downstream direction, respectively.

$$(\rho u)'_d = (\rho u)'_u \tag{25}$$

where ρ & u may be re-written as:

$$\rho = \bar{\rho} + \rho' \tag{26}$$

$$u = \bar{u} + u' \tag{27}$$

Applying this in general to the mass flux and neglecting second order perturbation terms:

$$(\rho u)' = \bar{\rho}\bar{u} + \bar{\rho}u' + \rho'\bar{u} + \cancel{\rho' u'} \tag{28}$$

Applying mass conservation across the pressure discontinuity (n.b. u & ρ are at $x = x_s$, ergo: $(u/c) = (u/c)_{x=x_s} = M_s$):

$$\bar{\rho}u_d^+ + \rho_d^+\bar{u} = \bar{\rho}u_u^- + \rho_u^-\bar{u} \tag{29}$$

Substituting Eqs. (20) and (23) into Eq. (29):

$$\cancel{\bar{\rho}}\left(\frac{p_d^+}{c\cancel{\bar{\rho}}}\right) + \left(\frac{p_d^+}{c^2}\right)\bar{u} = \cancel{\bar{\rho}}\left(\frac{-p_u^-}{c\cancel{\bar{\rho}}}\right) + \left(\frac{p_u^-}{c^2}\right)\bar{u} \tag{30}$$

Carrying out some additional algebra:

$$p_d^+(1 + M_s) = p_u^-(-1 + M_s) \tag{31}$$

$$p_d^+ = -p_u^-\left(\frac{1 - M_s}{1 + M_s}\right) \tag{32}$$

Recalling Eq. (24):

$$\Delta p = -p_u^-\left(\frac{1 - M_s}{1 + M_s}\right) - p_u^- = -p_u^-\left(\frac{2}{1 + M_s}\right) \tag{33}$$

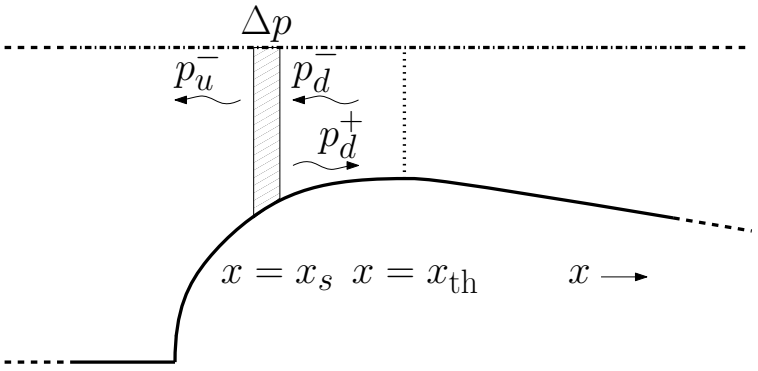

Fig. 5 Acoustic pressure waves emanating from a fluctuating pressure discontinuity Δp located at $x = x_s$ in the converging part of a choked nozzle. As the nozzle is choked and the flow is 1D, one has sonic line at $x = x_{\mathrm{th}}$, that is to say, in the throat.

$$p_u^- = -\frac{1 + M_s}{2}\Delta p \tag{34}$$

Similarly,

$$p_d^+ = \frac{1 - M_s}{2}\Delta p \tag{35}$$

where M_s is the Mach number at the sound source position x_s.

Moving forward it will be assumed that the above result obtained for a uniform cross-section duct can be applied in the subsonic parts of a choked nozzle with varying cross-sectional area $A = A(x)$. In this quasi-1D approximation A varies slowly in the flow direction, namely,

$$\frac{L_{\mathrm{nozzle}}}{A}\frac{\mathrm{d}A}{\mathrm{d}x} << 1. \tag{36}$$

where L_{nozzle} is the length of the nozzle.

The acoustic wave p_d^+ is partially reflected by the nozzle. Assuming quasi-steady behavior for this process, one can apply Eq. (5) to an isentropic pressure perturbation and after some algebra obtain an expression for the reflection coefficient which is defined as $R \equiv p_d^-/p_d^+$:

The reflection coefficient can be shown to be (see Appendix A)

$$R = \frac{1 - \frac{\gamma-1}{2}M_s}{1 + \frac{\gamma-1}{2}M_s} \tag{37}$$

The pressure fluctuation p_u' moving upstream from Δp is

$$p_u' = p_u^- + Rp_d^+ \tag{38}$$

Using Eqs. (34) and (35), one finds

$$p'_u = -\frac{\Delta p}{2}\left((1+M_s) - R\,(1-M_s)\right). \tag{39}$$

where M_s is the Mach number at $x = x_s$. The acoustic power emitted upstream is

$$|\Phi_s^-| = \frac{A_s}{\rho_s c_s}|p'_u|^2\,(1-M_s)^2\,. \tag{40}$$

At an upstream (observer) position $x = x_{\rm ob}$, the observed acoustic-power flow $|\Phi_{\rm ob}^-|$, is

$$|\Phi_{\rm ob}^-| = \frac{A_{\rm ob}}{\rho_{\rm ob} c_{\rm ob}}|p'_{\rm ob}|^2\,(1-M_{\rm ob})^2\,. \tag{41}$$

Taking the energy transport to $x = x_{\rm ob}$ to be lossless, namely, that $|\Phi_{\rm ob}^-| = |\Phi_s^-|$, one finds

$$|p'_{\rm ob}| = \sqrt{\frac{\rho_{\rm ob} c_{\rm ob}}{\rho_s c_s}\frac{A_s}{A_{\rm ob}}}\left((1+M_s) - R\,(1-M_s)\right)\left(\frac{1-M_s}{1-M_{\rm ob}}\right)\frac{\Delta p}{2} \tag{42}$$

Assuming an entropy "point particle," the excess mass is

$$m_e \equiv \int\limits_{V_e} \rho_e \mathrm{d}^3 x, \tag{43}$$

where the volume integral is taken over the volume of the entropy patch V_e. By virtue of Newton's second law, one has that the walls of the nozzle have to exert a force F_x on the flow to provide the acceleration of the "point particle"

$$F_x = m_e\left(u\frac{\mathrm{d}u}{\mathrm{d}x}\right) \tag{44}$$

From Curle's [14] analogy or Gutin's [15] principle, one knows that an unsteady force of a wall on the fluid is a source of sound. In this case, one may represent this dipolar sound source as the pressure discontinuity:

$$\Delta p = \frac{F_x}{A_s} \tag{45}$$

Substituting Eq. (45) in Eq. (42), yields

$$|p'_{\rm ob}| = \sqrt{\frac{\rho_{\rm ob} c_{\rm ob}}{\rho_s c_s}\frac{1}{A_{\rm ob} A_s}}\left((1+M_s) - R\,(1-M_s)\right)\left(\frac{1-M_s}{1-M_{\rm ob}}\right)\frac{m_e}{2}\left(u\frac{\mathrm{d}u}{\mathrm{d}x}\right). \tag{46}$$

Using Bernoulli's principle and isentropic perfect gas relations, one may find the following relations (see Appendix B & C) :

$$\boxed{\sqrt{\frac{\rho_{\rm ob}c_{\rm ob}}{\rho_s c_s}} = \left(\frac{1+\frac{\gamma-1}{2}M_s^2}{1+\frac{\gamma-1}{2}M_{\rm ob}^2}\right)^{\frac{\gamma+1}{4(\gamma-1)}}} \tag{47}$$

and

$$\boxed{\frac{A_s}{A_{\rm th}} = \frac{1}{M_s}\left(1+\frac{\gamma-1}{\gamma+1}(M_s^2-1)\right)^{\frac{\gamma+1}{2(\gamma-1)}}} \tag{48}$$

where $A_{\rm th} = 4S_1S_{\rm th}$ with S_1 and $S_{\rm th}$ the upstream half-duct height and the half height in the throat as defined in Fig. 6.

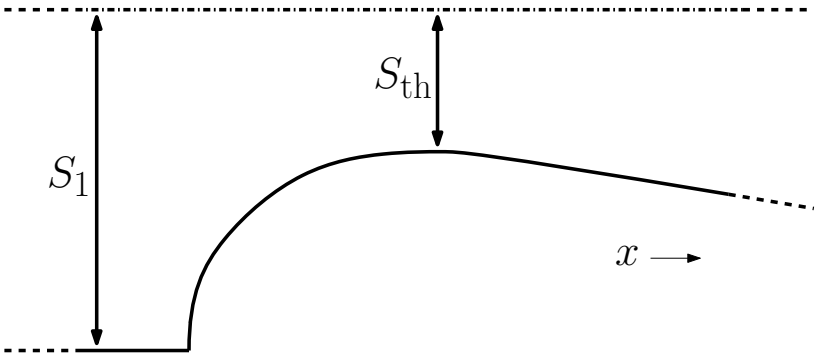

Fig. 6 S_1 **and** $S_{\rm th}$ **are the upstream half-duct height and the half height in the throat, respectively.**

The convective acceleration, ($u\mathrm{d}u/\mathrm{d}x$ in Eqs. (44) and (45)) can be estimated from two-dimensional (plane) numerical simulations of the stationary base flow (Appendix D). When such estimations are used in Eq. (45) the results will be said to have been obtained using the hybrid or inertial model.

In Fig. 7, results of this hybrid point-mass model are shown. These results are obtained by computing Eq. (46). The convective acceleration term $u(\partial u/\partial x)$ is obtained numerically (hence why this model is referred to as hybrid). Specifically, the dimensionless upstream observed acoustic response $|p'_{\rm ob}|S_1^3/(m_eU_1^2)$ is shown as a function of the dimensionless source position $(x_s - x_{\rm th})/S_1$ in the convergent part of the nozzle upstream from the throat position $x_{\rm th}$. The hybrid point-mass model results demonstrate sound is being produced throughout the nozzle, however, the majority of sound production occurs is primarily generated close to the throat, at around $(x_s - x_{\rm th})/S_1 = -0.1$.

III. Numerical simulations: methodology

Systematic studies of entropy-spot-choked-nozzle interaction were carried out using Hulshoff's specialised two-dimensional (plane) Euler Internal Aeroacoustics code (EIA) [16–18], which solves the compressible frictionless governing (Euler) equations:

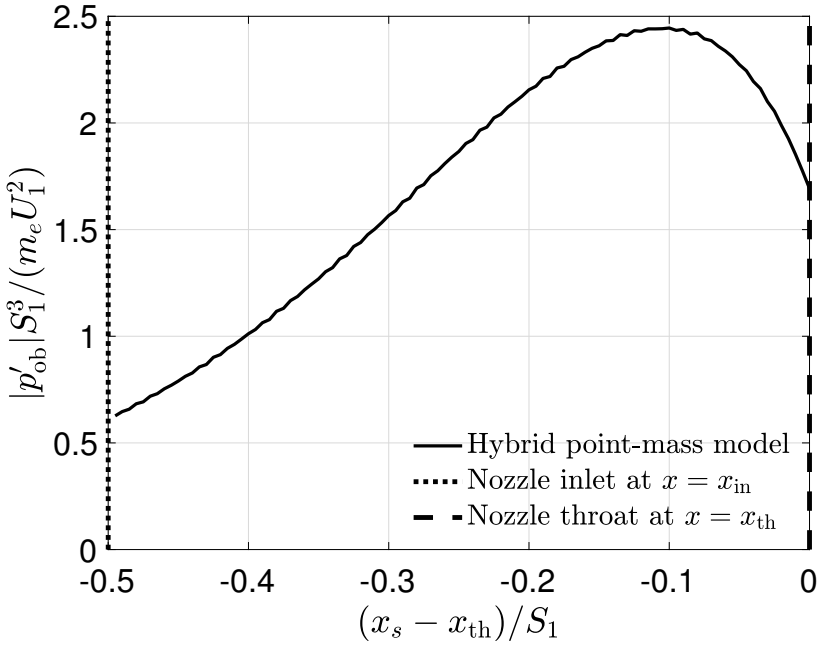

Fig. 7 Dimensionless upstream observed acoustic response $|p'_{\rm ob}|S_1^3/(m_e U_1^2)$ as a function of the dimensionless source position $(x_s - x_{\rm th})/S_1$ in the convergent part of the nozzle. The finely dotted and dashed vertical lines indicate the position of the nozzle inlet and throat, respectively.

$$\frac{\partial \rho}{\partial t} + \nabla \cdot (\rho \mathbf{u}) = 0 \tag{49}$$

$$\frac{\partial \rho \mathbf{u}}{\partial t} + \nabla \cdot (\rho \mathbf{u}\mathbf{u} + p\mathbf{1}) = \rho \mathbf{F}_E \tag{50}$$

$$\frac{\partial E_T}{\partial t} + \nabla \cdot ((E_T + p)\mathbf{u}) = Q_E \tag{51}$$

where $E_T = \rho(e + |\mathbf{u}|^2/2)$ is the total energy density, $\rho \mathbf{F}_E$ is an external momentum source density and Q_E is an external energy source. The energy source term Q_E was used to generate entropy patches. In conjunction with the heat capacity ratio $\gamma = 1.4$, the ideal gas law was used as an equation of state. It is noted that the external momentum source $\mathbf{F}_E$ can be used to generate vortices, as was done by Hulshoff et al. [17] and Hirschberg et al. [5–7]. Moreover, the methodology applied here is essentially the same as was reported by Hirschberg et al. [6, 19]; which were:

1) Computational meshes were generated.
2) A steady choked-nozzle base flow was established.
3) Unsteady entropy-spot-choked-nozzle-interaction simulations were performed, with the steady choked-nozzle base flow as an initial condition (IC). Namely, entropy patches (circular spots or rectangular slugs) were generated atop the IC.

In this section, the above steps are briefly expanded upon in §III.A, §III.B, and III.C, respectively.

Fig. 8 Geometry of the computational domain, with $S_1/S_{\text{th}} = 3$, used for the presently-presented study.

A. Computational mesh generation and information regarding numerical accuracy

In this subsection, details regarding mesh generation for the convergent-divergent-nozzle configuration used are provided. In Fig. 8, the computational domain's geometry for the configuration is shown. Which consists, from left to right, of: blocks 1 (green), 2 (red), 3 (yellow) and 4 (blue). Blocks 3 and 4 form a convergent-divergent nozzle with a contraction ratio: $S_1/S_{\text{th}} = 3$ (where $2S_1$ is upstream channel height and $2S_{\text{th}}$ is the height at the nozzle throat), which, for the choked-nozzle flows considered, corresponds to an upstream Mach number of $M = 0.20$.

To perform entropy-patch choked-nozzle interaction simulations: entropy patches were generated locally on block 1, in which it was ensured that cells produced during mesh-generation: had a square shape—to minimize small asymmetries (this is not strictly necessary however, it provides a slightly more symmetric solution to within the truncation error when using coarser meshes). The entropy patches were generated by application of a non-uniform external energy source Q_E (consult §III.C.2 for details) locally on this block. Block 2 served as a transition from the generation block to block 3. This was done to gradually change the mesh geometry whilst keeping the cells as square as possible. Block 3 contained the contraction part of the convergent-divergent nozzle (its inlet). The lower wall of the contraction in block 3 was generated using the Henrici transformation [20] for the analytical model (with contraction length $L_{\text{contraction}}/S_1 = 1/2$, for more info the reader is invited to consult Ref. [21]). Finally, one had, downstream from the contraction, block 4: the diverging part of said convergent-divergent nozzle (diffusor).

The number of points on the mesh was chosen to have a sufficient number of points (in each of the blocks) per spot radius R_s or half slug width $W_s/2$ of the entropy patch to ensure converged solutions. The spatial discretization used for the entropy-patch-nozzle-interaction simulations was based on a second-order total-variation-diminishing (TVD) Roe approximate Riemann solver with a van Leer limiter [22]. A five-stage Runge-Kutta time marching method was used for time integration. Using three meshes with 36, 54 and 81 points per $R_s/S_1 = 0.3$, Hirschberg et al. [5–7] determined: the estimated order-of-accuracy [23] to be 1.8 with a discretization error of approximately 1%. Ergo, for the purposes of the presently-reported study, meshes: were generated with at least 36 points per length-scale of the entropy patch used

to perform unsteady simulations. At this point it is noted that for the purposes of the presently reported work, an attempt to perform solution verification was performed and is discussed in III.C.3.

The same number of points on the left-hand (inlet) boundary of block 1 were used on the right-hand boundary of block 1 as well as the left- and right-hand boundaries of block 2. The change of a cell-surface area from cell to cell was kept as small as possible. Moreover, the number of points on the sides of the individual blocks was kept divisible by four to allow a three-level explicit multi-grid (EMG) method to be used to establish the base flow [16]. The initialization procedure of the choked-nozzle base flow is briefly described in the following subsection.

B. Establishment of a steady choked-nozzle base flow

Before unsteady entropy-patch choked-nozzle interaction could be studied, a steady choked-nozzle base flow had to be established on the computational domain (Fig. 8). Subsequently, this flow was used as an initial condition, atop which entropy patches were generated to investigate sound production due to entropy-patch choked-nozzle interaction. Generation of entropy patches and the applied boundary conditions for the unsteady simulations are discussed in §III.C.2. In this subsection, the establishment of the base flow is described.

The boundary conditions [16], which were imposed to establish said base flow where:

- A "usoft" boundary condition on the upstream wall (on the left-hand-side of Fig. 8). This boundary condition imposes:
  - a desired normal time averaged inflow velocity U_{des},
  - the local sound speed (which was set to 1 $\text{m} \cdot \text{s}^{-1}$),
  - the local density (which is set to $1\text{kg} \cdot \text{m}^{-3}$).
- Wall boundary conditions on the lower and upper walls of the channel (vanishing normal velocity).
- Connection boundary conditions on all the interfaces connecting the constituent blocks of the channel.
- A non-reflective boundary condition on the downstream domain boundary.

To determine the upstream inlet velocity, U_{des}, for a choked nozzle, the isentropic quasi-one-dimensional relation provided above was used Eq. (48). The equation was solved numerically to determine: which inlet Mach number needs to be imposed to ensure the establishment of a steady choked-nozzle base flow.

All the individual blocks of the mesh were assigned initial values of: the density, ρ_{initial}, the velocity $\mathbf{u}_{\text{initial}} = (u, v)$ and the pressure p_{initial}. On blocks 1, 2 and 3 the following values were imposed: $\rho_{\text{initial}} = 1$, $\mathbf{u}_{\text{initial}} = (U_{\text{des}}, 0)$ and $p_{\text{initial}} = c^2\rho_{\text{initial}}/\gamma$, where $\gamma = 1.4$ is the heat capacity for diatomic gas and c is the sound speed. c was set to 1 $\text{m} \cdot \text{s}^{-1}$ in the upstream blocks 1 and 2, by means of the "usoft" boundary condition [16]. On the downstream section of the mesh (block 4): $\rho_{\text{initial}} = 1$, $\mathbf{u}_{\text{initial}} = (1, 0)$ and $p_{\text{initial}} = c^2\rho_{\text{initial}}/(2\gamma)$ were imposed. Consequently, the pressure in block 4 was lower by a factor two compared to the upstream blocks 1, 2, and 3. This ensured that no shock-wave was formed downstream from the sonic line in the contraction, and that the ultimately-reached flow remained supersonic in block 4.

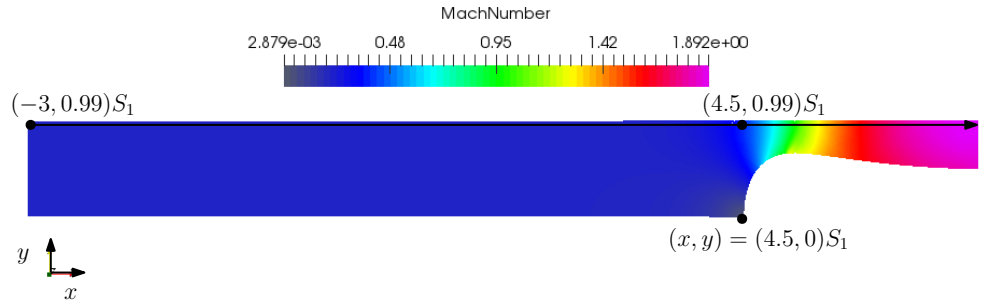

(a)

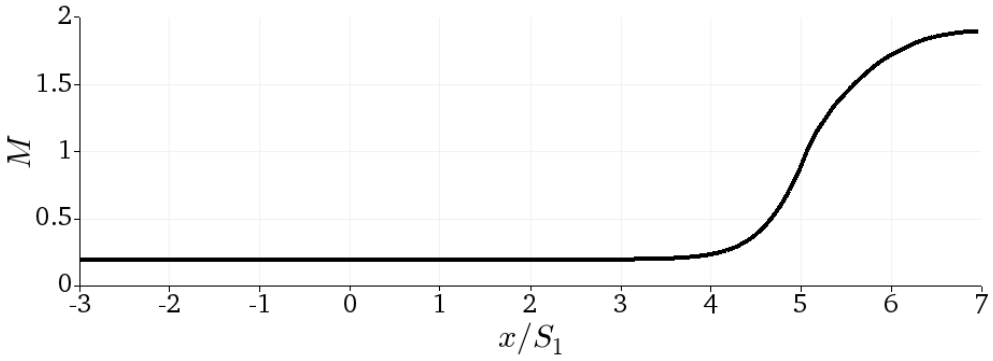

(b)

Fig. 9 Steady choked-nozzle base flow established for $S_1/S_{\text{th}} = 3$.

The initial condition base flow (IC) to be used for unsteady entropy-patch choked-nozzle interaction simulations was established using a three-level explicit multi-grid relaxation scheme. Spatial integration was performed using a second-order total-variation-diminishing (TVD) Roe approximate Riemann solver with a van Leer limiter [16, 22]. Time marching was done using: a (5,2) Runge-Kutta scheme with a Courant number $Co = 2$ [16]. The resulting IC for the contraction ratio $S_1/S_{\text{th}} = 3$ and an upstream inlet Mach number $M = 0.20$ is shown in Fig. 9.

C. Entropy-patch-nozzle-interaction simulations: boundary conditions and entropy-patch generation

In this subsection, the boundary conditions applied to carry out: unsteady entropy-patch choked-nozzle interaction simulations are reported (§III.C.1). Moreover, entropy-patch generation is succinctly covered in §III.C.2.

1. Boundary conditions, pressure-probe positions and emission time

The boundary conditions [16] applied for the unsteady entropy-patch-nozzle-interaction simulations, were:

- An acoustically non-reflective condition on the upstream wall (left-hand-side boundary on Fig. 8)—it:
  - mimics a connection to an infinite upstream channel,
  - maintains the local average inflow velocity, density and sound speed imposed by the base flow as an initial condition.
- A symmetry condition was applied on the dash-dotted boundary in Fig. 8.
- Connection boundary conditions on all the interfaces connecting the constituent blocks of the channel.
- Non-reflective boundary condition on the downstream end boundary (right-hand-side Fig. 8). Note: because a choked-nozzle flow was considered, the choice of outflow boundary condition was not critical (information cannot travel back upstream through a sonic line).
- Wall boundary conditions on the walls of the channel ($\mathbf{u} \cdot \mathbf{n} = 0$).

The acoustically non-reflective boundary conditions imposed on the upstream boundary of the computational domain allow one to record the upstream-traveling acoustic response due to entropy-patch-nozzle interaction, without: the interference of downstream-traveling spurious acoustic reflections. Indeed, if one had imposed boundary conditions which reflect acoustic waves, it would have been significantly more difficult to separate the upstream-traveling acoustic wave due to entropy-patch-nozzle interaction (the quantity of interest) & downstream traveling acoustic waves. The latter are due to reflections formed during the entropy-patch-generation phase. This methodology allows one to neatly separate the different events in time. Ergo, cogently separating the quantity of interest, in terms of time signal, from signals which are not pertinent.

To record the quantity of interest, the upstream acoustic response, p', a probe was placed at $\mathbf{x}_{\text{probe}} = (-2.75, 0.5)S_1$ close to the computational domain's upstream boundary (Fig. 10) to record: the pressure $p_{\text{probe}} = p_{\text{probe}}(t)$. The acoustic response was determined using $p' = p_{\text{probe}}(t) - p_{\text{probe}}(t_{\text{end}})$. The simulations were run for a time sufficiently

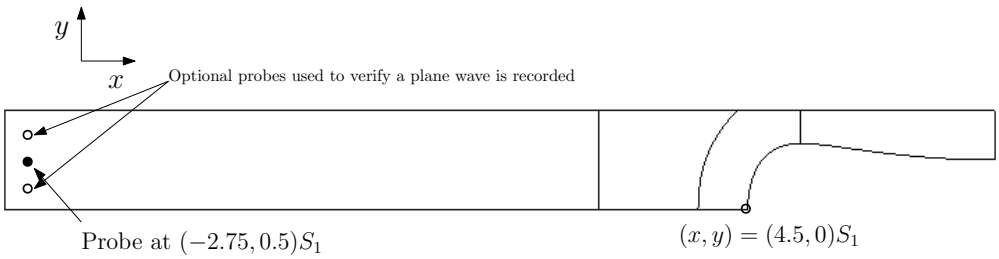

Fig. 10 Probe positions

long, to ensure that when $t = t_{\text{end}}$: one could assume that the flow field had returned to its stationary base-flow state. The acoustic response was determined to be a plane wave, by means of two additional probes, which were placed at $(-2.75, 0.52)S_1$ and $(-2.75, 0.75)S_1$ (indicated with the open circles in Fig. 10).

The travel time, t_t, the time the acoustic wave took to reach the probe coming from the nozzle, was estimated as follows:

$$t_t = \frac{|\mathbf{x}_{\text{probe}} - \mathbf{x}_{\text{th}}|}{c_1 - U_1} \tag{52}$$

where $|\mathbf{x}_{\text{probe}} - \mathbf{x}_{\text{th}}| = 7.25S_1$ is the distance from the nozzle inlet ($x_{\text{inlet}} = 4.5S_1$) to the probe ($x_{\text{probe}} = -2.75$). Using t_t, the retarded time is defined as follows:

$$t_r \equiv t - t_t \tag{53}$$

The upstream-recorded acoustic response signals, obtained from entropy-patch-nozzle-interaction simulations, will be presented as a function of t_r in §IV.

2. Entropy-patch generation

To generate a fully mature entropy patch—i.e., a slug or spot like the ones shown in Fig. 11—the energy-source term Q_E in Eq. (51) was used. The entropy patch was generated by means of localized energy injection around a point, which was convected with the base flow. The energy source Q_E was chosen to be the following a function of the user-set characteristic length of the to-be-generated entropy patch L_s—i.e., the spot radius R_s or the slug width W_s.

$$Q_E = \begin{cases} \frac{A_E}{2}\left(1 + \cos\left(\pi \frac{\zeta}{L_s}\right)\right) \text{ if } 0 \le \zeta \le L_s \\ 0 \text{ if } \zeta > L_s \end{cases} \tag{54}$$

where ζ is the distance from the source center, which moves with the flow. The amplitude A_E is the following function of time:

(a) Fully-mature entropy slug generated with $W_s/(2S_1) = 1.0$

(b) Fully-mature entropy spot generated with $R_s/S_1 = 1.0$

(c) Fully-mature entropy slug generated with $(W_s/(2S_1) = 3.0)$

(d) Fully-mature entropy spot generated with $(R_s/S_1 = 3.0)$

Fig. 11 Entropy field with fully-mature entropy patches.

$$\frac{2A_E}{A_{\max}} = \begin{cases} 1 - \cos\left(\frac{\pi t}{\tau_{\text{start}}}\right) \text{ if } 0 \le t \le \tau_{\text{start}} \\ 2 \text{ if } \tau_{\text{start}} < t \le \tau_{\text{start}} + \tau_{\max} \\ 1 + \cos\left(\frac{\pi(t-(\tau_{\text{start}}+\tau_{\max}))}{\tau_{\text{end}}}\right) \text{ if } \tau_{\text{start}} + \tau_{\max} < t \le \tau_{\text{start}} + \tau_{\max} + \tau_{\text{end}} \\ 0 \text{ for } \tau_{\text{start}} + \tau_{\max} + \tau_{\text{end}} < t < t_{\text{end}} \end{cases} \tag{55}$$

where the following parameters were user-set:

- $A_{\max}$, the maximum amplitude.
- τ_{start}, the lapse of time during which generation is initiated and smoothly ramped up.
- $\tau_{\max}$, the lapse of time during which entropy-patch generation is done with the maximum global amplitude.
- τ_{end}, the time during which the generation process is smoothly ramped down.
- t_{end}, the time at which entropy-patch generation ends.

I.e., entropy-patch generation comprises three phases, each of duration: τ_{start}, $\tau_{\max}$ and τ_{end}.

3. Solution verification

As previously specified in the §III.A meshes were generated with at least 36 points per length scale of the entropy patch on the basis of the works of Hirschberg et al. where very similar computational domain was used. Nevertheless, an

attempt to determine convergence and estimate numerical error in the presently reported work was made. An attempt to estimate the error was made via Richardson extrapolation (the reader is encouraged to consult for more details Appendix E).

Solution verification was attempted for the case of a circular entropy spot of $R_s/(2S_1) = 0.5$ by generating three meshes h_1, h_2, h_3 where h_2 is twice as fine compared to h_1, and h_3 being four times as fine compared to h_1 where h_1 was the original mesh generated containing 36 points per radius. Fig.12 shows the results of the recorded upstream acoustic pressure due to the interaction of an entropy spot with a choked-nozzle as a function of the simulation time t for the three grids generated.

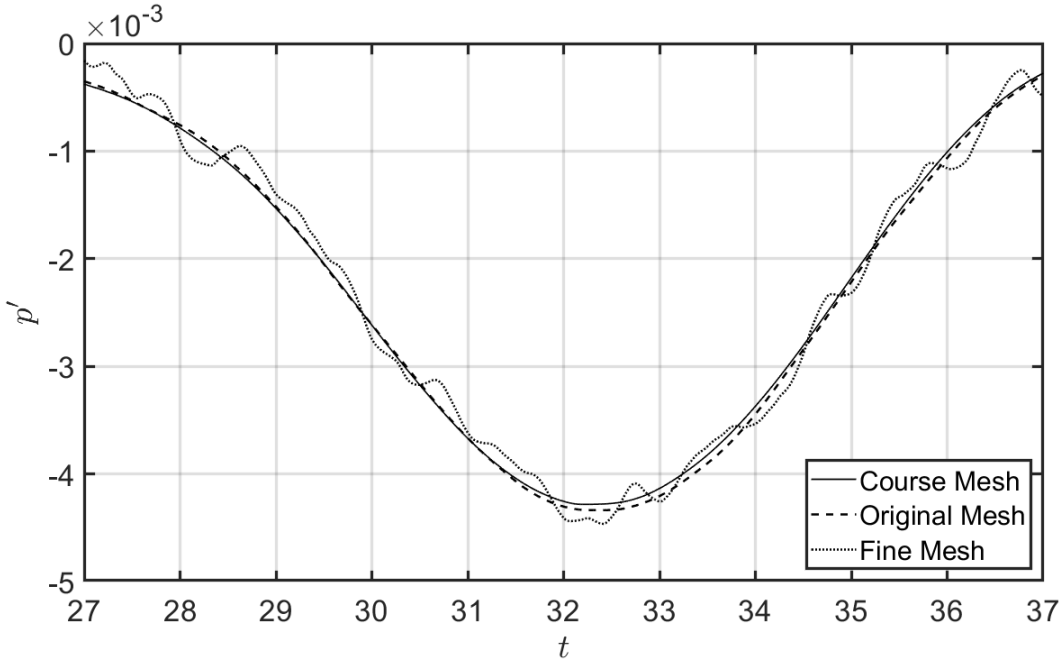

Fig. 12 Upstream acoustic response due to entropy patch choked-nozzle interaction

From the results of the "fine" mesh (refinement ratio of 4 with respect to the original mesh), one notices the presence of transient phenomena (or resonance) in the recorded response. This is likely due to the fact that the mesh is over-resolved for the specific simulation and therefore captures transient phenomena due to the unsteady generation of an entropy spot in the computational domain. In this case, the transient being captured is a standing half-wave ($\lambda/2$), which is the lowest longitudinal mode for a closed-closed pipe. This proves challenging in accurately estimating a value for the amplitude of the acoustic response, and consequently in accurately estimating the numerical error. It is noted that by allowing the simulation to run for longer time-steps, it is possible to allow transients to dissipate. However, as the Euler equations are highly non-dissipative in nature, this was not a viable approach.

In the process of solution verification, it became clear that it was possible to lower the number of points per radius

whilst still achieving convergence. More specifically, it was found that a convergent solution for the investigated problems could be obtained with as few as 18 points per radius of an entropy patch. This provides multiple benefits; coarser meshes may be produced, which is beneficial in terms of expedience and computational resources. Additionally, for the sake of solution verification, one avoids the problems of being over-resolved and thus transient phenomena are not captured. To this end, a second attempt at estimating the numerical error was performed. The "coarse" mesh was twice as coarse compared to the original mesh, and the "fine" mesh was twice as fine as the original mesh.

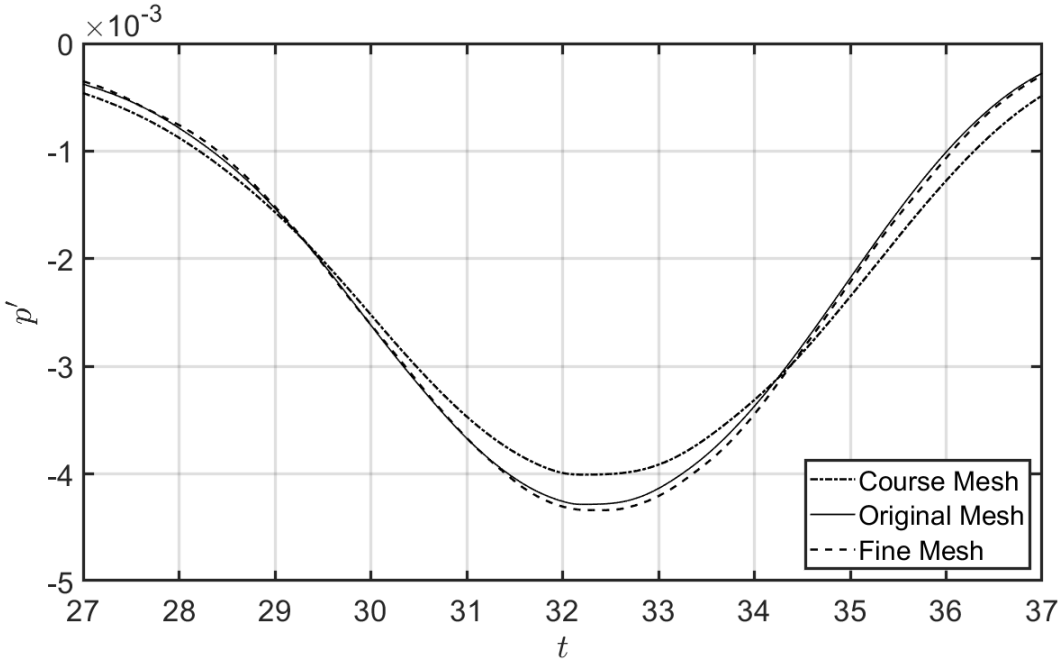

Fig. 13 Upstream acoustic response due to entropy patch choked-nozzle interaction

The results are shown in Fig.13. In this case the standing half-wave is not captured and enables an estimation of the numerical accuracy. Implementing the Richardson extrapolation (see Appendix E) the estimated numerical error was of 0.007%. This error is remarkably small and rather unrealistic. To confirm the results, the observed order of accuracy p_o was compared to the expected order of accuracy p. The expected order of accuracy is $p = 2$ as the simulation uses a second order spatial discretization. The expected order of accuracy p_o is significantly different and as discussed in Appendix E, the use of Richardson extrapolation is invalid.

In conclusion, attempts at estimating the numerical error were unsuccessful, nevertheless by visual inspection of Figs.12 & 13 one my assert that convergence is indeed achieved. Moreover, the prior works of Hirschberg et al. [5–7] which make use of the same methodology regarding mesh generation have successfully determined convergence and quantified the numerical error.

4. Effect of starting position of entropy patches

In this sub-section, the effects of the user-set starting position of the entropy patches is discussed. As previously mentioned, entropy-patch generation comprises three phases, the total duration of this generation period is 15s. Based on this, it is important to select an axial starting position such that the patch is given enough time to fully mature but at the same time not too much time such that the spot numerically dissipates before arriving at the nozzle inlet. Given that the spot is travelling with an axial velocity of $0.2\text{m} \cdot \text{s}^{-1}$ and the generation period is 15s, the distance the patch travels from before full maturity is, 3m which is also $3S_1$ given $S_1 = 1\text{m}$. Referring to Fig.10, the nozzle inlet is located at $x = 4.5$, this means that the minimum distance away from the inlet for entropy patch generation would be $x = 1.5$. Accounting for the fact that the entropy patches have an extent, the chosen starting point for entropy patch generation was set to $x = 0$. For very large entropy patches; namely, $L_s/(2S_1) \geq 1.5$ the starting position was shifted upstream to $x = -2$ to account for the larger extent of the patch.

The effect of the starting position of the entropy patch on the upstream acoustic response may be questioned. To this end, an investigation on the effect of varying the starting position of an entropy spot has been performed. More specifically, three simulations were performed for an entropy spot of $R_s/(2S_1) = 0.5$ where the starting position was varied between $x_{\text{start}} = -2$, $x_{\text{start}} = -1$ & $x_{\text{start}} = 0$. The results are presented in Fig.14 and clearly show that the effect of the starting position of the entropy patch on the upstream acoustic response is in fact negligible.

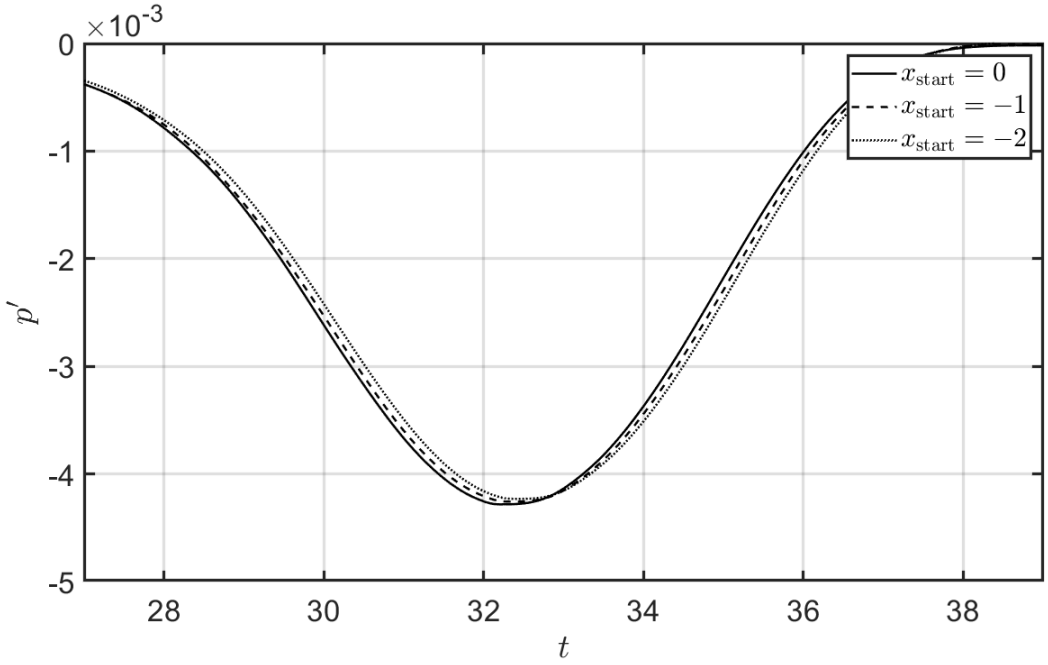

Fig. 14 Effect of entropy patch starting position on ECNI

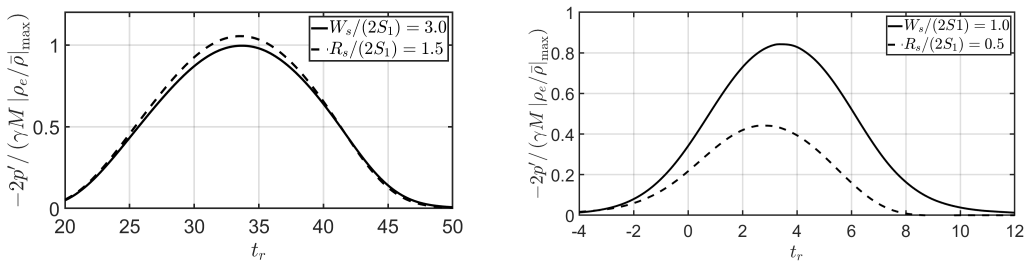

(a) (b)

Fig. 15 The upstream acoustic response scaled by the matching-conditions-model prediction vs. retarded time, for four patch sizes: (a) $R_s/(2S_1) = 1.5$ and $W_s/(2S_1) = 3.0$ & (b) $R_s/(2S_1) = 0.5$ and $W_s/(2S_1) = 1.0$.

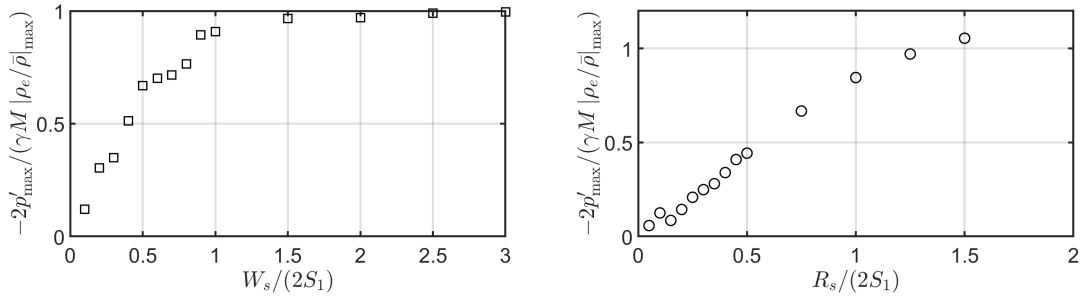

(a) Entropy slug (b) Entropy spot

Fig. 16 The upstream acoustic response amplitude vs. the entropy patch's normalized characteristic length.

IV. Numerical-simulation results and comparison to theory

A. Numerical-Simulation results compared to matching-conditions model

In Fig. 15, the upstream acoustic response p', scaled by the matching-condtion model prediction (Eq. (15)), is plotted as a function of time. To calculate the matching-conditions model prediction: the relative excess density $(\rho_e/\bar{\rho})$ was approximated by its amplitude $|\rho_e/\bar{\rho}|_{\max}$. Given that the entropy patches, which were generated, had negative excess density: $(\rho_e/\bar{\rho}) \simeq -|\rho_e/\bar{\rho}|_{\max}$ was used. Moreover, in Fig. 15: results obtained with two entropy-patch shapes—which were, an entropy slug (solid line) and spot (dashed line)—are compared. The results shown in Fig. 15(a) were obtained with $W_s/(2S_1) = 3.0$ (Fig. 11(c)) and $R_s/(2S_1) = 1.5$ ((Fig. 11(d))). Whereas the results in Figs. 15(b) where acquired using $W_s/(2S_1) = 1.0$ (Fig. 11(a)) and $R_s/(2S_1) = 0.5$ ((Fig. 11(b))). One observes that for $R_s/S_1 = W_s/(2S_1) = 3.0$ and $W_s/(2S_1) = 1.0$ the matching-conditions model yields: a remarkably good prediction (especially for $W_s/(2S_1) = 3.0$) for the amplitude $p'_{\max}$, which is the local extremum in p'.

That said, in Fig. 15(b), one observes a marked deviation from the matching-conditions-model prediction for the $R_s/(2S_1) = 0.5$ case. What's more, in Fig. 15(a), one observes a slight deviation of ca. 5%, between the matching-conditions-model predictions for the slug and the spot, respectively. It should be noted that the matching-conditions model is also quasi-1D in nature (§II.A), therefore, it cannot capture the effect of even subtle rounding of an entropy

patch's edges. This leads to reason that the shape and the size of the entropy patch affect sound production due to entropy-patch-nozzle interaction.

To confirm said reasoning: a series of cetris paribus simulations were carried out with various entropy-slug and -spot sizes; namely, $W_s/(2S_1)$ and $R_s/(2S_1)$ were varied. The results are shown in Figs. 16(a) and 16(b) for entropy slugs and spots, respectively. From data in Fig. 16 one gleans, matching-conditions modeling clearly captures the essence of sound production due to entropy patch nozzle interaction—provided that the characteristic length of the patch L_s, be it R_s or W_s, is about the same as or larger than the upstream-channel height. Ergo, in the case of a choked-nozzle flow for which $L_s/(2S_1) \gtrsim 1$: entropy-patch-nozzle interaction is dominated by matching-conditions effects—going forward, this will be referred to as the matching-conditions modeling regime.

B. Numerical-simulations result compared to inertial/hybrid model

For $L_s/(2S_1) \lesssim 1$, the data in Fig. 16, indicates that matching-conditions effects no longer dominate. With that in mind, it is reasoned that outside of said matching-conditions modeling regime, inertial effects start to play a non-negligible role. Moreover, it is hypothesized that there is an inertial modeling regime. Specifically, a regime where acceleration of the entropy patch through the choked nozzle plays an essential role in the establishment of the upstream acoustic response. Furthermore, it is reasoned that said inertial regime would be most likely be attained when one considers entropy patches of very small extent. In other words, if the entropy patch is quite small—namely, point-particle like or in Ffowcs-Williams & Howe's words: a "pellet"—the establishment of an upstream acoustic response would be dominated by inertial effects. In particular, in said inertial-modeling regime, convective acceleration would be the most consequential modeling ingredient.

To test the hypothesis re the existence of an inertial-modeling regime, the simulation results were compared to the quasi-one-dimensional point-mass model (or the hybrid model) proposed in §II.B. To do so, estimating the excess mass m_e carried by the entropy patch is needed—the reader is referred to Appendix F for more information on how this was done—in an unsteady entropy-patch-nozzle simulation.

In Fig. 17, the simulation's upstream acoustic-response amplitude p'_{max} is compared to its associated hybrid-model prediction p'_{hybrid}. In particular, $p'_{\text{max}}/p'_{\text{hybrid}}$ is shown as a function of the estimated excess mass $|m_e|/(S_1^3\bar{\rho})$ carried by the entropy patch.

One observes that as $|m_e|$ becomes smaller—i.e., the size of the patch becomes smaller—$p'_{\text{max}}/p'_{\text{hybrid}}$ becomes order one; that is to say, $p'_{\text{max}}/p_{\text{hybrid}} = \text{O}(1)$. This indicates, that there is indeed an inertial regime, and that it is reached, when: sufficiently small entropy patches—i.e., for spots $|m_e|/(S_1^3\bar{\rho}) \lesssim 10^{-2}$, which corresponds to $R_s/(2S_1) = 0.1$ & for slugs $|m_e|/(S_1^3\bar{\rho}) \lesssim 5 \times 10^{-2}$, which corresponds $W_s/(2S_1) = 0.2$—generate the upstream acoustic response as they are ingested by the choked nozzle.

The corollary to the data reflecting the existence of two clearly-distinct modeling regimes— namely, an inertial-

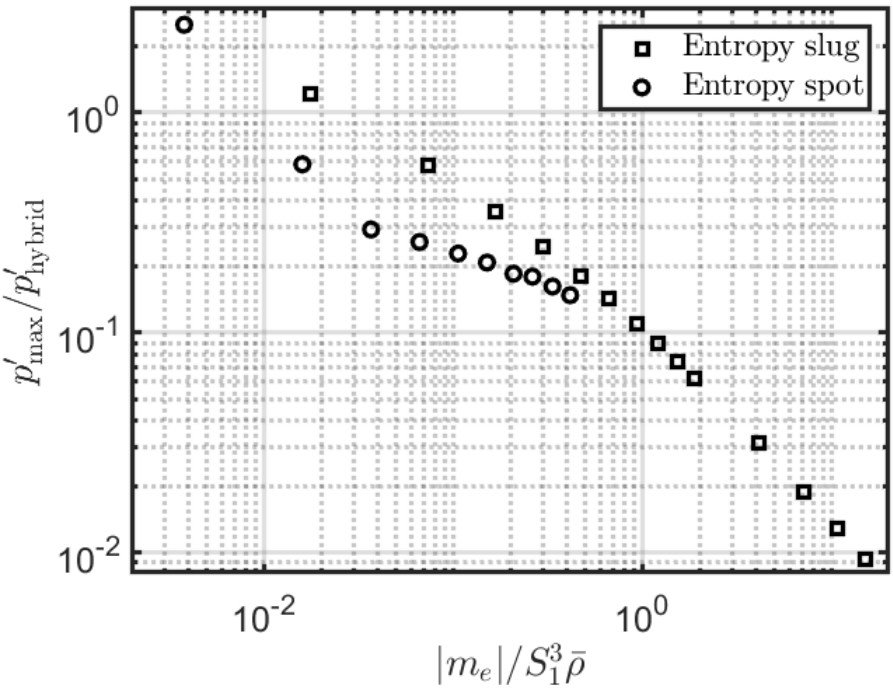

Fig. 17 Comparison of the simulation's upstream acoustic-response amplitude $p'_{\max}$ to the associated hybrid-model predictions p'_{hybrid} vs. the estimated excess mass $|m_e|$ carried by the entropy patch.

modeling regime for small enough entropy patches ($W_s/(2S_1) \lesssim 0.2$ & $R_s/(2S_1) \lesssim 0.1$) and a matching-conditions modeling regime for large enough patches ($L_s/(2S_1) \gtrsim 1$)—is, that there is a regime between the aforementioned two regimes. Moreover, it is posited: in said connecting regime a blend of matching-conditions and inertial effects play a role in the generation of an upstream acoustic response due to entropy-patch-nozzle interaction. Going forward, this posited regime will be referred to as: the blended-physical-effects regime.

This leads to conclude: in the case of entropy-patch choked-nozzle interaction size and shape do matter.

C. Preliminary results re effect of amplitude contained within entropy patches

In addition to the investigations presented above, the effect of varying the maximum amplitude $A_{\max}$ contained within an entropy patch on the models' prediction was investigated. Two distinct cases were investigated:

- $A_{\max}$ varied for $R_s/(2S_1) = 0.05$
- $A_{\max}$ varied for $R_s/(2S_1) = 1.5$

$A_{\max}$ was varied in order of magnitudes of the original user-set amplitude.

- For $R_s/(2S_1) = 1.5$, $A_{\max}$ assumed values of 0.003, 0.03, 0.3
- For $R_s/(2S_1) = 0.05$, $A_{\max}$ assumed values 0.002, 0.003, 0.03, 0.3

where $A_{\max} = 0.03$ was the original amplitude chosen for all unsteady ECNI simulations.

The preliminary results of these simulations were subsequently compared to the matching-conditions & inertial model to evaluate whether the amplitude contained within an entropy patch is influential on the model prediction.

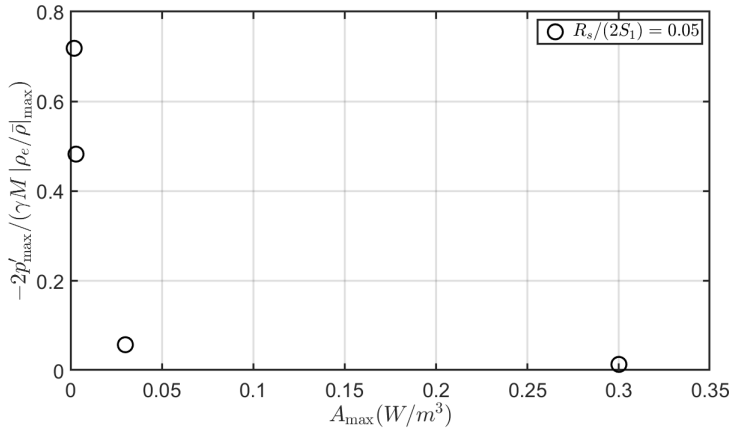

Fig. 18 Effect of amplitude variation on matching-conditions model prediction for entropy spot $R_s/S_1 = 0.1$

Fig.18 shows the results of varying the maximum amplitude contained within an entropy spot $R_s/(2S_1) = 0.05$. The results are rather remarkable, as they clearly show that the maximum amplitude contained within an entropy patch is undoubtedly influential on the matching-conditions model prediction. For the case $A_{\max} = 0.003$ a solid prediction (approximately 70%) for the upstream acoustic response by the matching-conditions model is obtained. This is despite the fact that $R_s/(2S_1) = 0.05$ is clearly outside of the matching-conditions modelling priorly established.

Similarly, the results presented in Fig.19 confirm that indeed the amplitude is consequential to the matching-conditions model prediction. In both cases, one may point out, that as the maximum amplitude contained within an entropy spot decreases, the matching-conditions model yields a better prediction of the upstream acoustic response due to entropy patch choked-nozzle interactions.

The effect of varying the amplitude is also evaluated with respect to the inertial model. The results of varied-amplitude unsteady ECNI simulations for spots $R_s/(2S_1) = 0.05$ are compared to the inertial model. This procedure is not done for the spot $R_s/(2S_1) = 1.5$ as in this case the spot is too large and does not fully fit in the computational domain, in that regard, determining the excess mass for such a spot is rather difficult. The results of the comparison with the inertial model are presented in Fig.20. The preliminary results again confirm that the maximum amplitude contained within an entropy spot clearly have an influence on the model prediction of the upstream acoustic response. However, in the case of the inertial model, as the amplitude decreases, a worse prediction for the acoustic response is obtained. This contradicts the observations for the matching-conditions model. In both cases, what can indubitably be said is: the maximum amplitude contained within entropy spots plays an effect in the upstream acoustic responses predicted by both the matching-conditions model and the inertial model.

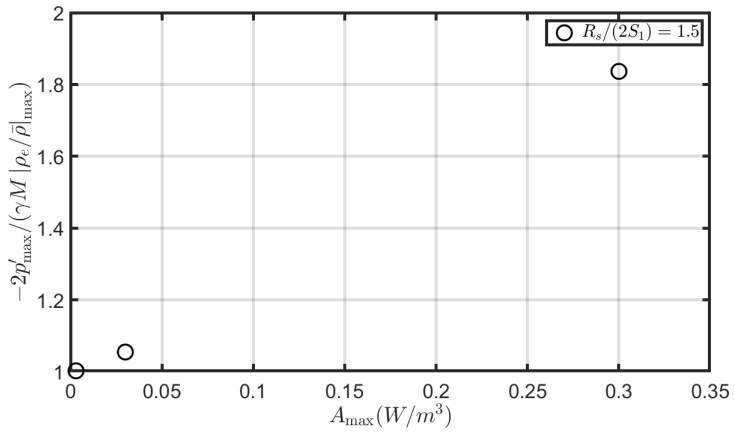

Fig. 19 Effect of amplitude variation on matching-conditions model prediction for entropy spot $R_s/S_1 = 3.0$

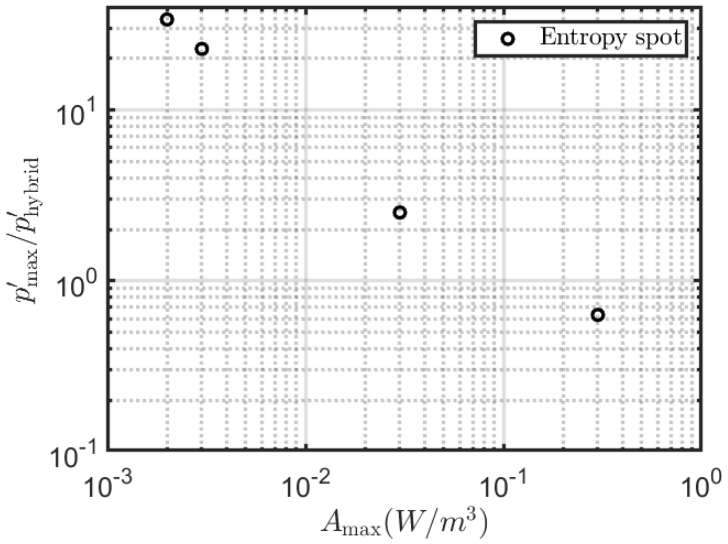

Fig. 20 Effect of amplitude variation on inertial model prediction for entropy spot $R_s/(2S_1) = 0.05$

V. Conclusion

Analysis of dedicated numerical simulations presented in this paper shows that, in the case choked-nozzle flows when the characteristic length of the entropy patch L_s is roughly the same as or larger than the upstream channel height: sound production due to entropy-patch-nozzle interaction is clearly dominated by matching-conditions effects. Ergo, if $L_s/(2S_1) \gtrsim 1$ the entropy-patch-nozzle interaction is said to be in the matching-conditions-modeling regime. Sound production due to the passage of two types of entropy patches moving through a nozzle atop a steady-choked-nozzle flow were investigated; namely, rectangular slugs and circular spots. All the slugs had a height equal to that of the channel upstream from the choked nozzle. In both cases, the size of the patches was varied by changing its characteristic length (the width of the slug W_s or the radius of the spot R_s). The presented analysis indicates that for small enough

entropy patches, $R_s/(2S_1) \lesssim 0.1$ and $W_s/(2S_1) \lesssim 0.2$, inertial effects govern the production of the upstream acoustic response. It is proposed that this regime be referred to as the inertial-modeling regime. In addition, the data reflect that the aforementioned regimes are clearly-distinct. Ergo, it is posited that: there is a regime between said two regimes, which is proposed to be called: the blended-physical-effects regime. In the later regime, it is hypothesized that: a blend of matching-conditions and inertial effects play a role in the generation of an upstream acoustic response due to entropy-patch-nozzle interaction.

Moreover, preliminary results on the maximum amplitude contained within entropy spots highlight the marked influence of said amplitude on matching-conditions & inertial modelling predictions. These results show that the matching-conditions model yields better predictions for the upstream acoustic response as the maximum amplitude contained within an entropy spot decreases. This is the case at least for spots with a characteristic length of $R_s/(2S_1) = 0.05$ & $R_s/(2S_1) = 1.5$. Conversely, the inertial model seems to yield better predictions when the maximum amplitude contained within an entropy spot increases; at least for an entropy spot of extent $R_s/(2S_1) = 0.05$.

A. Derivation of Reflection coefficient

Recalling some fundamental equations:

$$\frac{c'}{c} = \frac{u'}{u} \tag{56}$$

$$p' = c^2\rho' = p^+ + p^- \tag{57}$$

$$u' = (p^+ + p^-)\frac{1}{\rho c} \tag{58}$$

$$c^2 = \gamma\frac{p}{\rho} \tag{59}$$

Taking the natural logarithm of Eq. (59) and differentiating yields:

$$2\frac{c'}{c} = \frac{p'}{p} - \frac{\rho'}{\rho} = \frac{p'}{p} - \frac{p'}{\rho c^2} = \frac{p'}{p}\left(1 - \frac{1}{\gamma}\right) \tag{60}$$

Dividing both sides by 2 and re-writing the term inside the brackets:

$$\frac{c'}{c} = \frac{p'}{2p}\left(1 - \frac{1}{\gamma}\right) = \frac{p'}{2p}\left(\frac{\gamma - 1}{\gamma}\right) \tag{61}$$

Rewriting the pressure perturbation in terms of an upstream and downstream component gives:

$$\frac{p'}{2p}\left(\frac{\gamma - 1}{\gamma}\right) = \frac{p^+ + p^-}{2p}\left(\frac{\gamma - 1}{\gamma}\right) \tag{62}$$

Using the Mach number:

$$\frac{p^+ + p^-}{2p}\left(\frac{\gamma - 1}{\gamma}\right) = \frac{p^+ + p^-}{\gamma p M} \tag{63}$$

Multiplying both sides by γp:

$$(p^+ + p^-)\frac{(\gamma - 1)}{2} = \frac{1}{M}(p^+ - p^-) \tag{64}$$

Rewriting to include the definition of R:

$$p^+(1 + R)\frac{\gamma - 1}{2} = \frac{p^+}{M}(1 - R) \tag{65}$$

Dividing both sides by p^+ and moving M to the other side:

$$(1 + R)\frac{(\gamma - 1)}{2}M = 1 - R \tag{66}$$

Expanding the LHS:

$$\frac{\gamma-1}{2}M + \frac{\gamma-1}{2}MR = 1 - R \tag{67}$$

Factoring out R:

$$R\left(1 + \frac{\gamma-1}{2}M\right) = 1 - \frac{\gamma-1}{2}M \tag{68}$$

and finally solving for R yields:

$$\boxed{R = \frac{1 - \frac{\gamma-1}{2}M_s}{1 + \frac{\gamma-1}{2}M_s}} \tag{69}$$

B. Derivation of Eq. (47)

For a calorically perfect gas, one has:

$$\mathrm{d}h = C_p \mathrm{dT} = \frac{1}{\rho}\mathrm{d}p \tag{70}$$

which may be re-written as:

$$C_p \mathrm{d}T = RT\frac{\mathrm{d}p}{p} \tag{71}$$

Rearranging to solve for $\mathrm{d}T/T$:

$$\frac{\mathrm{d}T}{T} = \frac{\gamma-1}{\gamma}\frac{\mathrm{d}p}{p} \tag{72}$$

The equation of state is:

$$p = \rho RT \tag{73}$$

taking the natural logarithm and differentiating:

$$\frac{\mathrm{d}p}{p} = \frac{\mathrm{d}\rho}{\rho} + \frac{\mathrm{d}T}{T} \tag{74}$$

Substituting 72 into the above expression yields:

$$\frac{\mathrm{d}\rho}{\rho} = \frac{\mathrm{d}T}{T}\left(\frac{\gamma}{\gamma-1}\right) - \frac{\mathrm{d}T}{T} = \left(\frac{1}{\gamma-1}\right)\frac{\mathrm{d}T}{T} \tag{75}$$

Integration yields:

$$ln\left(\frac{\rho_0}{\rho}\right) = ln\left(\left(\frac{T_0}{T}^{\frac{1}{\gamma-1}}\right)\right) \tag{76}$$

which can be written as:

$$\frac{\rho_0}{\rho} = \left(\frac{T_0}{T}\right)^{\frac{1}{\gamma-1}} \tag{77}$$

What can also be shown, using the definition of the speed of sound for a calorically perfect gas is:

$$\frac{c_0}{c} = \sqrt{\frac{T_0}{T}} \tag{78}$$

which, using the isentropic relation for the total temperature can be re-written as follows:

$$c_0 c = \sqrt{\frac{T_0}{T}} = \left(\left(1 + \frac{\gamma - 1}{2}\right) M^2\right)^{1/2} \tag{79}$$

Knowing all of this, deriving Eq. (47) is rather straight-forward:

$$\frac{\rho_{ob}}{\rho_s}\frac{c_{ob}}{c_s} = \left(\frac{T_{ob}}{T_s}\right)^{\frac{1}{\gamma-1}} \left(\frac{T_{ob}}{T_s}\right)^{1/2} \tag{80}$$

$$= \frac{T_{ob}}{T_s}^{\frac{\gamma+1}{2(\gamma-1)}} = \left(\frac{1 + \frac{\gamma-1}{2}M_s^2}{1 + \frac{\gamma-1}{2}M_{ob}^2}\right)^{\frac{\gamma+1}{2(\gamma-1)}} \tag{81}$$

$$\boxed{\sqrt{\frac{\rho_{\mathrm{ob}} c_{\mathrm{ob}}}{\rho_s c_s}} = \left(\frac{1 + \frac{\gamma-1}{2}M_s^2}{1 + \frac{\gamma-1}{2}M_{\mathrm{ob}}^2}\right)^{\frac{\gamma+1}{4(\gamma-1)}}} \tag{82}$$

C. Derivation of Eq. (48)

The derivation follows from the generalised isentropic relations presented here for convenience:

$$\frac{p_0}{p} = \left[1 + \frac{\gamma - 1}{2} M^2\right]^{\frac{\gamma}{\gamma-1}} \tag{83}$$

$$\frac{\rho_0}{\rho} = \left[1 + \frac{\gamma - 1}{2} M^2\right]^{\frac{1}{\gamma-1}} \tag{84}$$

$$\frac{c_0}{c} = \left[1 + \frac{\gamma - 1}{2} M^2\right]^{\frac{1}{2}} \tag{85}$$

$$\frac{T_0}{T} = \left[1 + \frac{\gamma - 1}{2} M^2\right] \tag{86}$$

as well as the sonic conditions (indicated by the superscript *) for a choked flow which are obtained by imposing $M = 1$ in the isentropic relations:

$$\frac{p^*}{p_0} = \left[\frac{2}{\gamma+1}\right]^{\frac{\gamma}{\gamma-1}} \tag{87}$$

$$\frac{\rho^*}{\rho_0} = \left[\frac{2}{\gamma+1}\right]^{\frac{1}{\gamma-1}} \tag{88}$$

$$\frac{c^*}{c} = \left[\frac{2}{\gamma+1}\right]^{\frac{1}{2}} \tag{89}$$

$$\frac{T^*}{T_0} = \left(\frac{2}{\gamma+1}\right) \tag{90}$$

From mass conservation, it holds that:

$$\frac{A}{A^*} = \frac{\rho^*}{\rho}\frac{V^*}{V} = \frac{\rho^*}{\rho_0}\frac{\rho_0}{\rho}\frac{V^*}{V} \tag{91}$$

Combining the appropriate isentropic and sonic conditions yields:

$$\frac{A}{A^*} = \frac{A}{A_{th}} = \frac{1}{M}\left[\frac{2}{\gamma+1}\left(1+\frac{\gamma-1}{2}M^2\right)\right]^{\frac{\gamma+1}{2(\gamma-1)}} \tag{92}$$

which with algebra may be re-written into the desired form:

$$\boxed{\frac{A_s}{A_{\text{th}}} = \frac{1}{M_s}\left(1+\frac{\gamma-1}{\gamma+1}(M_s^2-1)\right)^{\frac{\gamma+1}{2(\gamma-1)}}} \tag{93}$$

D. Hybrid point-mass model: convective acceleration estimation

As was alluded to in section II.B, one can estimate the convective acceleration term $u\mathrm{d}u/\mathrm{d}x$ in Eq. (46) from the stationary base flow simulation result. To do this the Paraview functions "plot over line" and "spreadsheet view" were used to extract the velocity data along the line between points $(x_{\text{in}}, 0.99S_1)$ and $(x_{\text{th}}, 0.99S_1)$ as sketched in Fig. 21. The extraction line is sketched in Fig. 21 as a black arrow in the streamwise direction. The spatial coordinates and velocity data are exported as comma separated value files using the "export spreadsheet" functionality in Paraview's "spreadsheet view." The values were extracted form a hundred equidistant points each separated by a distance ΔX. The data were loaded into Matlab with the "readscv" function, and two arrays $\mathbf{X}$ and $\mathbf{U}$ with horizontal coordinates and velocity were defined. The convective acceleration array $\mathbf{A}_c$ was then estimated, as follows:

$$A_{c,i} = U_i\frac{U_i - U_{i-1}}{\Delta X} \tag{94}$$

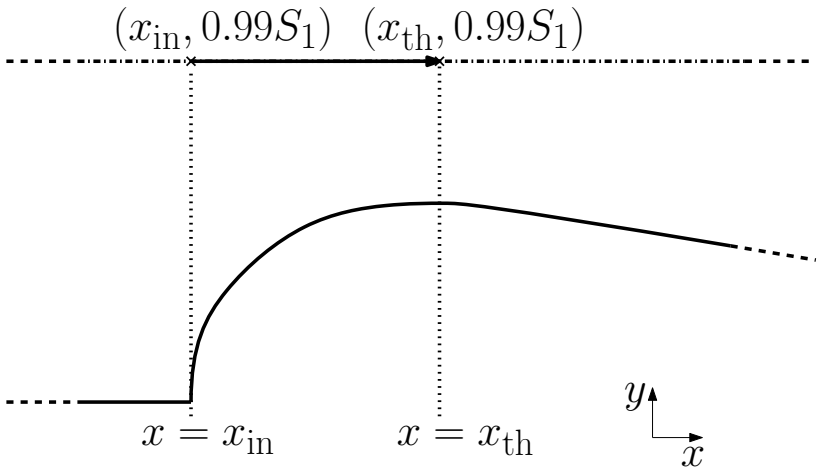

Fig. 21 Sketch of line over which coordinates and velocity data were extracted with Paraview.

where the subscript i represent the i^{th} array element.

E. Richardson Extrapolation

The following information is obtained from [23]. Assuming one has a method which is p-th order accurate, a value for the solution may be written as:

$$f_d = f_e + gh^p + O(h^{p+1}) \tag{95}$$

where f_e is the exact solution, g is a function of the gradients of the continuos solution and h is the step size. Considering a mesh spacing ratio between a fine mesh h_1 and a coarser mesh h_2:

$$r = \frac{h_2}{h_1} \tag{96}$$

Replacing h_1 by h Eq.95 may be written for the solution of both meshes:

$$f_1 = f_e + gh^p + O(h^{p+1}) \tag{97}$$

$$f_2 = f_e + g(rh)^p + O((rh)^{p+1}) \tag{98}$$

$$\tag{99}$$

Neglecting higher order terms, an estimate for the exact solution may be obtained:

$$f_e = f_1 + \frac{f_1 - f_2}{r^p - 1} \tag{100}$$

such that an estimate of the discretisation error may be obtained:

$$\epsilon = f_e - f_1 = \frac{f_1 - f_2}{r^p - 1} \tag{101}$$

One must note that the above only applies if the meshes h_1 & h_2 lie in the asymptotic region of the discretisation. In order to confirm the following, the observed order of accuracy p_o should be equal to the expected order of accuracy p. This may be determined via a third mesh h_3 where $h_3 = rh_2$. This may be used to solve for p_o:

$$p_o = \frac{\ln\left(\frac{f_3 - f_2}{f_2 - f_1}\right)}{\ln(r)} \tag{102}$$

If p_o differs significantly from p then the use of Richardson extrapolation is invalid.

F. Excess-mass estimation

In this appendix an estimation of the the excess mass m_e carried by the entropy patch is provided. Said excess mass defined, as follows:

$$m_e \equiv \int_{V_e} \rho_e \mathrm{d}^3 x \tag{103}$$

in §F.A and §F.B this a relation used to estimate m_e for circular spots and rectangular slug are derived, respectively.

A. Excess mass circular spot

Based on the density distribution in a mature spot, the judgment is made that a Gaussian distribution for ρ_e can be assumed. Thus, one has:

$$\rho_e = \rho_{e,\mathrm{ext}} \exp\left(-\frac{x^2 + y^2}{R_s^2}\right) = \rho_{e,\mathrm{ext}} \exp\left(-\frac{r^2}{R_s^2}\right) \tag{104}$$

Defining the upstream-channel width $W_c = S_1$. Moreover, assuming an unbounded space—i.e., not taking into account spots with a radius larger than half the upstream-channel height. One can estimate the excess mass in a circular spot, as follows:

$$m_e \simeq W_c \int_{-\infty}^{\infty} \int_{-\infty}^{\infty} \rho_e \mathrm{d}x\mathrm{d}y \tag{105}$$

which can obviously be rewritten as

$$m_e \simeq W_c \int_0^\infty \rho_e 2\pi r \mathrm{d}r \tag{106}$$

Substituting Eq. (104), one finds:

$$\begin{aligned} m_e &\simeq W_c \rho_{e,\mathrm{ext}} \int_0^\infty \exp\left(-\frac{r^2}{R_s^2}\right) 2\pi r \mathrm{d}r & (107)\\ &= W_c \rho_{e,\mathrm{ext}} \pi R_s^2 \int_0^\infty \exp\left(-\frac{r^2}{R_s^2}\right) \mathrm{d}\left(\frac{r^2}{R_s^2}\right) & (108) \end{aligned}$$

which yields

$$m_e \simeq W_c \rho_{e,\mathrm{ext}} \pi R_s^2 = S_1 \rho_{e,\mathrm{ext}} \pi R_s^2 \tag{109}$$

B. Excess mass rectangular slug

Based on the density distribution in a mature slug, it is judged that a Gaussian distribution for ρ_e can be assumed. Ergo, one has:

$$\rho_e = \rho_{e,\mathrm{ext}} \exp\left(-\frac{x^2}{(W_s/2)^2}\right) \tag{110}$$

Taking upstream-channel height $H_c = 2S_1$ and its width is $W_c = S_1$, the excess mass can be estimated as follows:

$$\begin{aligned} m_e &\simeq W_c H_c \int_{-\infty}^\infty \rho_e \mathrm{d}x & (111)\\ &= W_c H_c \rho_{e,\mathrm{ext}} \int_{-\infty}^\infty \exp\left(-\frac{x^2}{(W_s/2)^2}\right) \mathrm{d}x & (112)\\ &= W_c H_c \rho_{e,\mathrm{ext}} I_{\mathrm{int}} & (113) \end{aligned}$$

where

$$I_{\mathrm{int}} = \int_{-\infty}^\infty \exp\left(\frac{x^2}{(W_s/2)^2}\right) \mathrm{d}x \tag{114}$$

Taking the square of I_{int}, one has

$$
\begin{aligned}
I_{\text{int}}^2 &= \int_{-\infty}^{\infty} \exp\left(-\frac{x^2}{(W_s/2)^2}\right) \mathrm{d}x \\
&= \int_{-\infty}^{\infty} \exp\left(-\frac{x^2}{(W_s/2)^2}\right) \mathrm{d}x \int_{-\infty}^{\infty} \exp\left(-\frac{y^2}{(W_s/2)^2}\right) \mathrm{d}y \\
&= \int_{-\infty}^{\infty}\int_{-\infty}^{\infty} \exp\left(-\frac{x^2+y^2}{(W_s/2)^2}\right) \mathrm{d}x\mathrm{d}y \\
&= \int_{0}^{\infty} \exp\left(-\frac{r^2}{(W_s/2)^2}\right) 2\pi \mathrm{d}r = \pi\left(\frac{W_s}{2}\right)^2
\end{aligned} \tag{115}
$$

Taking the square-root of this result, yields:

$$
I_{\text{int}} = \sqrt{\pi}\left(\frac{W_s}{2}\right) \tag{116}
$$

Substituting this result in Eq. (113), one finds:

$$
m_e \simeq W_c H_c \sqrt{\pi}\left(\frac{W_s}{2}\right)\rho_{e,\text{ext}} = S_1^2\sqrt{\pi} W_s \rho_{e,\text{ext}} \tag{117}
$$

Acknowledgments

I would like to express my gratitude for the support offered by the Engineering Fluid Dynamics group (chaired by Kees Venner) in terms of the academic supervision. I would like to give a special thank you to my supervisor Lionel Hirschberg for the continuous supervision throughout this assignment. I would like to thank the co-authors who contributed to the academic publication of this work. I would like to thank Avraham Hirschberg for the thoughtful & meaningful conversations about the presently-reported work. I would like to thank my parents & my girlfriend for being beside me every step of the way and always pushing me to be the best version of myself.

References

[1] Morgans, A. S., and Duran, I., "Entropy Noise: A Review of Theory, Progress and Challenges," *International Journal of Spray and Combustion Dynamics*, Vol. 8, No. 4, 2016, pp. 285–298. doi:10.1177/1756827716651791.

[2] Dotson, K. W., Koshigoe, S., and Pace, K. K., "Vortex Shedding in a Large Solid Rocket Motor Without Inhibitors at the Segmented Interfaces," *Journal of Propulsion and Power*, Vol. 13, No. 2, 1997, pp. 197–206. doi:10.2514/2.5170.

[3] Hulshoff, S. J., Hirschberg, A., and Hofmans, G. C. J., "Sound production of vortex nozzle interactions," *Journal of Fluid Mechanics*, Vol. 439, 2001, pp. 335–352. doi:10.1017/S0022112001004554.

[4] Anthoine, J., Buchlin, J.-M., and Hirschberg, A., "Effect of Nozzle Cavity on Resonance in Large SRM: Theoretical Modeling," *Journal of Propulsion and Power*, Vol. 18, No. 2, 2002, pp. 304–311. doi:10.2514/2.5935.

[5] Hirschberg, L., Hulshoff, S. J., Collinet, J., Schram, C., and Schuller, T., "Vortex nozzle interaction in solid rocket motors: A scaling law for upstream acoustic response," *Journal of the Acoustical Society of America*, Vol. 144, No. 1, 2018, pp. EL46–EL51. doi:10.1121/1.5046441.

[6] Hirschberg, L., Hulshoff, S. J., Collinet, J., Schram, C., and Schuller, T., "Influence of Nozzle Cavity on Indirect Vortex- and Entropy-Sound Production," *AIAA Journal*, Vol. 57, No. 7, 2019, pp. 3100–3103. doi:10.2514/1.J058138.

[7] Hirschberg, L., and Hulshoff, S. J., "Lumped-Element Model for Vortex-Nozzle Interaction in Solid Rocket Motors," *AIAA Journal*, Vol. 58, No. 7, 2020, pp. 3241–3244. doi:10.2514/1.J058673.

[8] Dowling, A. P., and Mahmoudi, Y., "Combustion Noise," *Proceedings of the Combustion Institute*, Vol. 35, No. 1, 2015, pp. 65–100. doi:10.1016/j.proci.2014.08.016.

[9] NASA, "NASA facts: Making future commercial aircraft quieter." *Technical Report FS-1999-07-003-GRC*, 1999.

[10] Commission, E., for Mobility, D.-G., Transport, for Research, D.-G., and Innovation, *Flightpath 2050 – Europe's vision for aviation – Maintaining global leadership and serving society's needs*, Publications Office, 2011. doi:doi/10.2777/50266.

[11] Marble, F. E., and Candel, S. M., "Acoustic disturbance from gas non-uniformities convected through a nozzle," *Journal of Sound and Vibration*, Vol. 55, 1977, pp. 225–243. doi:10.1016/0022-460X(77)90596-X.

[12] Ffowcs Williams, J. E., and Howe, M. S., "The generation of sound by density inhomogeneities in low Mach number nozzle flows," *Journal of Fluid Mechanics*, Vol. 70, No. 3, 1975, pp. 605–622. doi:10.1017/S0022112075002224.

[13] Kowalski, K., Hulshoff, S. J., Ströer, P., Withag, J., Genot, A., Morgans, A. S., Bake, F., Venner, K., Sanders, M., and Hirschberg, L., "Entropy-Patch-Choked-Nozzle Interaction: Quasi-Steady-Modeling-Regime Limits Probed," *30th AIAA/CEAS Aeroacoustics Conference (2024)*, 2024. doi:10.2514/6.2024-3113, URL https://arc.aiaa.org/doi/abs/10.2514/6.2024-3113.

[14] Curle, N., "The influence of solid boundaries upon aerodynamic sound," *Proc. Roy. Soc. A*, Vol. 231, 1955, pp. 505–514. doi:https://doi.org/10.1098/rspa.1955.0191.

[15] Pierce, A. D., *Acoustics: an introduction to its physical principles and applications*, Acoustical Society of America, Melville, New York, USA, 1994.

[16] Hulshoff, S. J., *EIA an Euler Code for Internal Aeroacoustics: method description and user's guide*, Faculty of Aerospace Engineering, Delft University of Technology, Delft, the Netherlands, October 2016.

[17] Hulshoff, S. J., Hirschberg, A., and Hofmans, G. C. J., "Sound production of vortex nozzle interaction," *Journal of Fluid Mechanics*, Vol. 439, 2001, pp. 335–352.

[18] Hirschberg, L., Hulshoff, S. J., Schuller, T., Schram, C. F., and Collinet, J., *Numerical simulations based evidence of impingement free sound production during vortex-nozzle interaction in solid rocket motors*, AIAA, 2019. doi:10.2514/6.2019-2421, URL https://arc.aiaa.org/doi/abs/10.2514/6.2019-2421.

[19] Hirschberg, L., "Low order modeling of vortex driven self-sustained pressure pulsations in solid rocket motors," Ph.D. thesis, CentraleSupélec, Université Paris-Sacly, 2019.

[20] Henrici, P., *Applied and Computational Complex Analysis*, Vol. I, Wiley-Interscience, NY, USA, 1974.

[21] Hirschberg, L., Schuller, T., Schram, C., Collinet, J., Yiao, M., and Hirschberg, A., "Interaction of a vortex with a contraction in a 2-dimensional channel: incompressible flow prediction of sound pulse," *23rd AIAA/CEAS Aeroacoustics conference*, 2017.

[22] Venkatakrishnan, V., and Jameson, A., "Computation of unsteady transonic flows by the solution of Euler equations," *AIAA Journal*, Vol. 26, No. 8, 1988, pp. 974–981.

[23] Hulshoff, S. J., *Computational modelling: lecture notes*, TU Delft, 2016.